COMMUNICATION

Check for updates

Constructing nanoneedle arrays of heterostructured RuO$_2$–Co$_3$O$_4$ with tip-effect-induced enrichment of reactants for enhanced water oxidation†

Xu Zhang,[a] Junnan Song,*[a] Tongming Sun,[b] Minmin Wang, [ID][b] Jinli Zhu,[b] Yang Yu*[c] and Jiacheng Wang [ID]*[a]

Nanoneedle arrays of heterostructured RuO$_2$–Co$_3$O$_4$ electrocatalysts were constructed, showing improved water oxidation activity and durable stability. The synergy of tip-effect-induced OH$^-$ enrichment, superior hydrophilicity, and heterojunction-enhanced electron transfer promotes water oxidation activity.

Hydrogen is widely regarded as the most environmentally friendly alternative to fossil fuels. Electrocatalytic water splitting is one of the most promising strategies for sustainable hydrogen production to meet future energy demands.[1] However, the sluggish kinetics of the oxygen evolution reaction (OER) severely hinder the overall efficiency of water splitting.[2] Although Ru-based and Ir-based materials are currently the state-of-the-art OER catalysts, their high cost and natural scarcity present significant barriers to industrial-scale implementation.[3,4] This challenge highlights the urgent need to develop OER catalysts that combine high efficiency, long-term stability, and economic viability.

Notably, heterointerface engineering enables precise tuning of catalyst electronic configurations, optimal modulation of intermediate adsorption strength, and consequent activity enhancement.[5] For example, Mu *et al.* reported that defective RuO$_2$/TiO$_2$ nanoheterostructures provide 10 mA cm^{-2} at an overpotential of 296 mV for the alkaline OER.[6] Sun *et al.* reported a rutile-structured Ru–Sn solid-solution oxide (Ru$_{0.6}$Sn$_{0.4}$O$_2$) displaying a low overpotential of 245 mV to reach 10 mA cm^{-2} in 1.0 M KOH electrolyte.[7] Additionally, the construction of nanoneedle arrays provides dual functional benefits: (1) improving hydrophilicity to accelerate mass transport

processes,[8] and (2) obtaining high-curvature nanostructures with tip-enhanced local electric fields that concentrate electrolyte ions and reactants at active sites. This combined effect simultaneously reduces reaction barriers and facilitates rapid mass transfer to active sites, ultimately boosting catalytic activity.[9] Thus, it is expected that high-performance RuO$_2$-based electrocatalysts could be prepared by integrating heterojunction and morphology engineering. In addition, spinel Co$_3$O$_4$ with low cost and abundant active sites is considered to be a promising catalyst for the OER, which can improve the activity by adjusting the electronic structure and local structure. Bo and coworkers constructed Co$_3$S$_4$@Co$_3$O$_4$/NSC core@ shell nanostructures as bifunctional ORR/OER electrocatalysts for rechargeable Zn–air batteries. The interfaces between Co$_3$S$_4$@Co$_3$O$_4$ and Co$_3$O$_4$/NSC could improve conductivity, and accelerate charge transfer.[10] Jin *et al.* developed a heterogeneous Co$_3$O$_4$/CeO$_2$ nanocomposite to modify the electronic structure of Co$_3$O$_4$ and establish an improved local bonding environment by introducing CeO$_2$, consequently modifying the redox characteristics of Co and enhancing the acidic OER performance.[11] Therefore, simply constructing heterojunction structures and focusing on the surface reconstruction between multiple metal oxide surfaces could improve the OER activity for hydrogen economy.

Herein, we synthesized RuO$_2$ nanoparticle-decorated Co$_3$O$_4$ nanoneedle arrays on nickel foam (NF) through a sequential process involving Co$_3$O$_4$ growth, Ru^{3+} ion exchange, and subsequent annealing. The resulting RuO$_2$/Co$_3$O$_4$ heterostructure exhibits outstanding OER electrocatalytic performance in alkaline media, achieving a low overpotential of 223 mV at 100 mA cm^{-2} with remarkable stability exceeding 100 hours of continuous operation. XPS analysis shows that electrons transfer from RuO$_2$ to Co$_3$O$_4$ at the heterogeneous interface, resulting in electron redistribution, which can optimize OER energetics. The nanoneedle architecture simultaneously enhances surface hydrophilicity, accelerating mass transport. Furthermore, the densely arranged Co$_3$O$_4$ nanoneedles bind to enhance the local electric field effect induced by the tip, promoting OH$^-$ enrichment at active sites while exposing additional catalytic centers.

[a] *Zhejiang Key Laboratory for Island Green Energy and New Materials, Institute of Electrochemistry, School of Materials Science and Engineering, Taizhou University, Taizhou 318000, Zhejiang, China. E-mail: jnsong@nuaa.edu.cn, jiacheng.wang@tzc.edu.cn*

[b] *College of Chemistry and Chemical Engineering, Nantong University, Nantong 226019, Jiangsu, China*

[c] *School of Pharmaceutical Sciences, Taizhou University, Taizhou 318000, Zhejiang, China. E-mail: yuyang430@tzc.edu.cn*

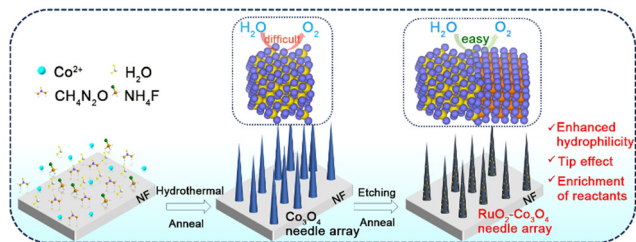† Electronic supplementary information (ESI) available. See DOI: https://doi.org/10.1039/d5cc01933h

Fig. 1 Schematic drawing of heterostructured RuO₂/Co₃O₄ needle-array electrocatalysts for efficient OER.

This dual mechanism facilitates efficient O_2 evolution and significantly enhances alkaline OER kinetics. Our findings provide fundamental insights into the electronic structure modulation of heterostructured catalysts and contribute to the development of cost-effective catalytic systems for practical water electrolysis.

Fig. 1 shows the decoration of Co_3O_4 nanoneedle arrays with RuO_2 nanoparticles. The synthesis begins with the thermal conversion of cobalt carbonate hydroxide (CoCH) into a Co_3O_4 scaffold structure. Subsequently, the obtained Co_3O_4 substrates undergo controlled ion exchange reactions in an aqueous $RuCl_3$ solution for varying durations, followed by calcination under ambient conditions to produce the final RuO_2/Co_3O_4 electrocatalyst. Dynamic contact angle measurements (Fig. S1, ESI†) reveal the superior hydrophilicity of the RuO_2/Co_3O_4 electrocatalyst compared to bare NF. Upon water droplet contact ($t = 0$ s), complete surface wetting occurred within 0.073 seconds for the composite catalyst, demonstrating rapid electrolyte penetration, which facilitates optimal electrode–electrolyte interfacial contact. In addition, the rough nanoneedles formed by loaded nanoparticles can cause sharp tip enhancement and proximity effects, and generate stronger electric fields, which are conducive to the enrichment of OH^- around the active site, optimizing the reaction energy barrier, and promoting the release of O_2 bubbles, thereby improving the OER process.[12]

The surface morphology of the catalysts was examined using field-emission scanning electron microscopy (FESEM). The as-prepared CoCH precursor exhibited smooth nanoneedle-like structures with a diameter of approximately 3–4 μm (Fig. S2, ESI†). After calcination to form Co_3O_4, the nanoneedle architecture remained largely intact (Fig. S3, ESI†). Subsequent Ru^{3+} ion exchange followed by calcination produced RuO_2/Co_3O_4 heterostructures, which preserved the nanoneedle morphology while exhibiting uniformly anchored RuO_2 nanoparticles on the surface, resulting in a roughened nanostructure (Fig. 2a–c). This well-defined nanoneedle configuration maximizes the exposure of active sites, enhances electrolyte infiltration, facilitates bubble release, and ensures structural stability during prolonged oxygen evolution reaction (OER).[13]

Transmission electron microscopy (TEM) further confirmed the unique nanowire-like structure of RuO_2/Co_3O_4 (Fig. 2d). High-resolution TEM (HRTEM) analysis revealed lattice spacings of 0.28 nm and 0.31 nm (Fig. 2e), corresponding to the (220) plane of Co_3O_4 and the (110) plane of RuO_2, respectively. High-angle annular dark-field TEM (HAADF-TEM) imaging, coupled with
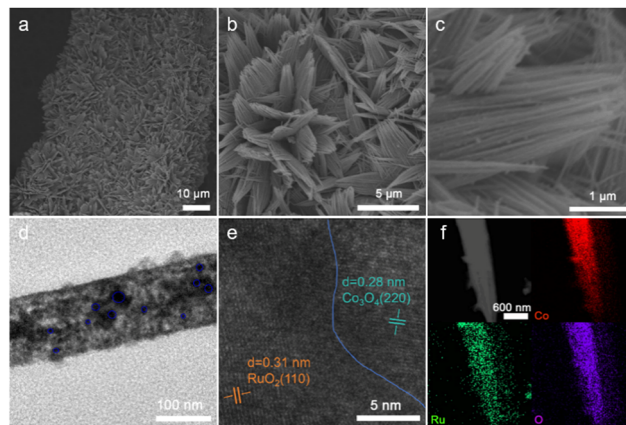

Fig. 2 (a)–(c) SEM, (d) TEM, (e) HRTEM, and (f) EDX mapping images of RuO_2/Co_3O_4 needle-arrays.

elemental mapping (Fig. 2f), demonstrated the homogeneous spatial distribution of Ru, Co, and O throughout the whole needle, conclusively verifying the formation of RuO_2/Co_3O_4 heterogeneous nanoneedles.

The heterostructure of RuO_2/Co_3O_4 was analyzed using X-ray diffraction (XRD, Fig. 3a). It shows distinct diffraction peaks at 31.2°, 36.8°, 44.8°, 59.3°, and 65.2°, corresponding to the (220), (311), (400), (511), and (440) planes of cubic Co_3O_4 (JCPDS no. 09-0418). Additional peaks at 28.0°, 35.0°, and 54.3° align with the (110), (101), and (211) planes of tetragonal RuO_2 (JCPDS no. 43-1027), confirming the successful formation of the heterostructure.

The electronic structure of RuO_2/Co_3O_4 was investigated by X-ray photoelectron spectroscopy (XPS, Fig. 3b). In the Co 2p XPS spectra (Fig. 3c), two significant peaks of pristine Co_3O_4 located at 779.3 and 794.3 eV belong to Co^{3+}, while another two peaks positioned at 780.5 and 795.5 eV are attributed to Co^{2+}. In the spinel structure of Co_3O_4, Co^{2+} is located at a tetrahedral position, while Co^{3+} cations are located in octahedral sites.[14] Compared to Co_3O_4, the binding energies of RuO_2/Co_3O_4 exhibit a negative shift of ca. 0.5 eV. As displayed in Fig. 3d,
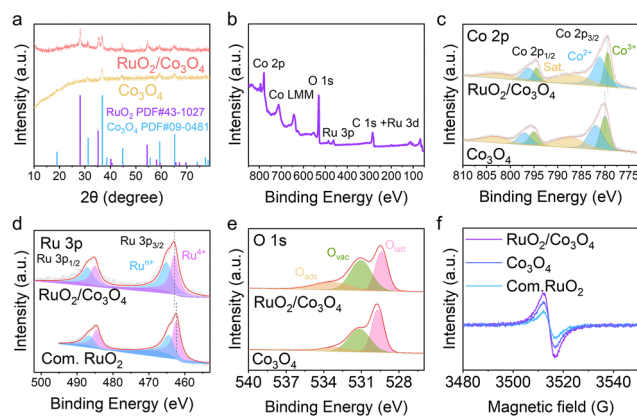

Fig. 3 (a) XRD patterns of RuO_2/Co_3O_4 and Co_3O_4. (b) The whole XPS spectrum of RuO_2/Co_3O_4. (c)–(e) The XPS spectra of (c) Co 2p, (d) Ru 3p, and (e) O 1s for RuO_2/Co_3O_4. (f) Electron paramagnetic resonance of RuO_2/Co_3O_4, com. RuO_2 and Co_3O_4.

the Ru 3p XPS spectra show two pairs of spin–orbit double peaks located at around 462.9 and 465.1 eV for Ru $3p_{3/2}$ and 485.1 and 487.2 eV for Ru $3p_{1/2}$, which are assigned to the Ru^{4+} and $Ru^{>4+}$ species.[15] Compared to commercial RuO_2, the binding energies of RuO_2/Co_3O_4 exhibit a positive shift of *ca.* 0.6 eV, implying a partial charge transfer between RuO_2 and Co_3O_4, which can be attributed to the strong support and active phase synergy effect. Deconvolution of the O 1s spectra (Fig. 3e) identifies three components: lattice oxygen (O_{latt}, 529.3 eV), oxygen vacancies (O_{vac}, 531.0 eV), and adsorbed water (O_{ads}, 533.4 eV).[16] Among them, the oxygen vacancy content of RuO_2/Co_3O_4 increased by 4% compared with cobalt tetroxide. This result is confirmed by the electron paramagnetic resonance (EPR) spectrum (Fig. 3f). This vacancy enrichment likely originates from charge compensation during Ru^{3+} ion exchange. Collectively, these results demonstrate significant electronic restructuring at the RuO_2/Co_3O_4 interface. The synergistic interaction between the phases can optimize the water dissociation kinetics and intermediate adsorption/desorption energetics, thereby accelerating overall water electrolysis efficiency.[17]

The OER activity of RuO_2/Co_3O_4 was systematically evaluated in 1 M KOH using a conventional three-electrode system, with comparative studies against pristine RuO_2/Co_3O_4 and commercial RuO_2. Linear sweep voltammetry (LSV) curves were *iR*-corrected and normalized to the reversible hydrogen electrode (RHE). The Ru content in RuO_2/Co_3O_4 was precisely controlled by varying ion-exchange durations, with inductively coupled plasma optical emission spectrometer (ICP-OES) analysis confirming the optimized mass ratio (Table S1, ESI†). After 9 hours of ion exchange, the catalyst exhibited peak performance, characterized by a high electrochemical active surface area (ECSA) and low charge-transfer resistance (Fig. S4 and S5, ESI†). As illustrated in Fig. 4a, RuO_2/Co_3O_4 requires an exceptionally low overpotential of 223 mV to deliver 100 mA cm^{-2}, significantly surpassing RuO_2/Co_3O_4 (350 mV) and commercial RuO_2 (400 mV). Impressively, even at a high current density of 200 mA cm^{-2}, RuO_2/Co_3O_4 maintains superior performance with minimal overpotential (Fig. 4b), outperforming benchmark catalysts across all tested current densities. Reaction kinetics analysis reveals a Tafel slope of 46.46 mV dec^{-1} for RuO_2/Co_3O_4, markedly lower than Co_3O_4 (70.66 mV dec^{-1}) and commercial RuO_2 (87.63 mV dec^{-1}) (Fig. 4c), confirming accelerated OER kinetics enabled by hetero-interface engineering. Electrochemical impedance spectroscopy (EIS) further corroborates this enhancement, with RuO_2/Co_3O_4 exhibiting the smallest semicircle diameter (Fig. 4d), indicative of reduced charge-transfer resistance and faster interfacial kinetics. The ECSA, derived from double-layer capacitance (C_{dl}) measurements *via* cyclic voltammetry at varying scan rates (Fig. S6, ESI†), reaches 328.95 mF cm^{-2} for RuO_2/Co_3O_4, exceeding Co_3O_4 (167.60 mF cm^{-2}) and commercial RuO_2 (40.68 mF cm^{-2}) by factors of 1.96 and 8.09, respectively (Fig. 4e).[18] This substantial increase in C_{dl} directly correlates with electronic structure modulation at the RuO_2/Co_3O_4 heterointerface, which exposes abundant active sites and enhances charge-transfer efficiency.

The enhanced electrocatalytic activity may be attributed to the tip effect of the rough nanoneedles.[12] Densely packed
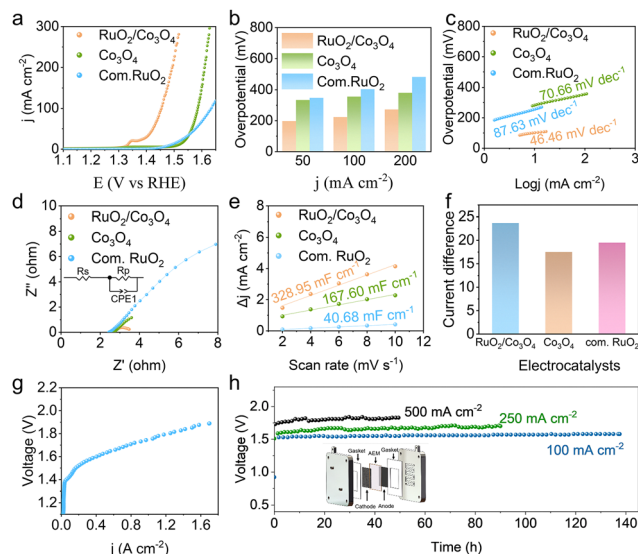

Fig. 4 (a) LSV curves, (b) overpotentials at 50, 100 and 200 mA cm^{-2}, (c) corresponding Tafel slopes, (d) EIS Nyquist plots, and (e) capacitive current density against the scan rate of RuO_2/Co_3O_4, Co_3O_4, and com. RuO_2 in 1.0 M KOH. (f) Current difference between the polarization curves in 1.0 M KOH solution with and without 1.0 M methanol for RuO_2/Co_3O_4, Co_3O_4 and com. RuO_2. (g) Polarization curves of RuO_2/Co_3O_4, which were measured by the use of an AEMWE cell in 1.0 M KOH with a scan rate of 10 mV s^{-1}. (h) Chronopotentiometric measurements of stability at 0.5 A cm^{-2}, 0.25 A cm^{-2} and 0.1 A cm^{-2}. Inset is a diagram of an AEMWE electrolyzer.

nanoneedles can induce a strong local electric field, enriching OH^- ions at the electrode surface, exposing more active sites to OH^- ions, and promoting O_2 release, thus accelerating the alkaline oxygen evolution reaction (OER) process. To verify the enrichment of OH^- ions, methanol molecular probe experiments were conducted (Fig. S7, ESI†). The methanol oxidation reaction (MOR) follows a well-established mechanism in which methanol molecules nucleophilically attack electrophilic *OH species.[19,20] The nucleophilic reagent methanol can easily adsorb the electrophilic reagent *OH in the process of the OER, which forms a competitive relationship with the adsorption of *OH by the OER. Therefore, the MOR is considered as an electronic probe assaying the adsorption of OER intermediates, that is, the increase of current density in the MOR is positively correlated with the coverage of intermediate *OH.[21,22] The difference in current density due to the MOR is proportional to the charge transferred, which can be quantified by calculating the area between the curves (Fig. 4f). The current difference between the MOR and OER on RuO_2/Co_3O_4 nanoneedles is greater than that observed on Co_3O_4 and RuO_2, indicating a stronger MOR competitive reaction and validating enhanced *OH adsorption on RuO_2/Co_3O_4. To demonstrate the stability of RuO_2/Co_3O_4 in an alkaline environment, the catalyst stability was tested at a current density of 100 mA cm^{-2}. The voltage degradation of RuO_2/Co_3O_4 was found to be negligible after 100 hours (Fig. S8, ESI†).

After the OER stability test, a series of characterizations were executed to minutely explore the morphology or structure evolutions of the spent catalyst. XPS was also carried out to

investigate the chemical state and surface composition of the oxide after the stability test (Fig. S9, ESI†). It can be seen that the binding energy of Ru 3p has undergone a slight positive shift, indicating that Ru has undergone a slight oxidation during the OER process. SEM analysis was used to observe micro-morphological changes after testing, revealing that the nanowire array remained largely intact and that Ru, Co, and O elements were uniformly distributed throughout the catalyst (Fig. S10, ESI†), highlighting the robustness of the catalyst. Notably, the OER performance of RuO_2/Co_3O_4 outperforms most recently reported Ru-containing electrocatalysts (Fig. S10 and Table S2, ESI†). In addition, we used custom anion exchange membrane electrolysis (AEMWE) cells to evaluate water decomposition performance in alkaline media with high current density. Under continuous operation, the RuO_2/Co_3O_4 based AEMWE only needs 1.723 V battery voltage to achieve 1 A cm^{-2} water decomposition current density (Fig. 4g). To assess its industrial relevance, extended stability tests were performed at current densities of 0.1, 0.25, and 0.5 A cm^{-2} (Fig. 4h). The cell demonstrated excellent long-term stability, with negligible voltage fluctuations during 120 hours of operation, confirming the structural integrity and corrosion resistance of the RuO_2/Co_3O_4 catalyst under harsh alkaline conditions. These results suggest that RuO_2/Co_3O_4 exhibits excellent OER activity and significant stability due to the presence of abundant heterogeneous interfaces and densely packed nanoneedles.

In summary, we have developed highly efficient and stable RuO_2/Co_3O_4 heterogeneous nanoneedle electrocatalysts through an ion exchange reaction and a simple pyrolysis method. The optimal RuO_2/Co_3O_4 electrocatalyst achieves a minimal overpotential of 223 mV at 100 mA cm^{-2}. Furthermore, it exhibits exceptional OER stability, with no significant degradation observed at 100 mA cm^{-2} over 100 hours, outperforming most recently reported state-of-the-art electrocatalysts. The experimental results demonstrate that the heterogeneous interface facilitates strong electron interactions, enhancing the OER activity. Additionally, the methanol oxidation molecular probe test confirms that the densely packed nanoneedles promote the enrichment of OH$^-$ ions around the active sites, exposing more active sites to OH$^-$ ions, thereby accelerating the release of O$_2$ bubbles. This study presents a viable approach for producing high-performance transition metal oxide catalysts for efficient water oxidation.

Data availability

Data available within the article or its ESI.†

Conflicts of interest

There are no conflicts to declare.

Notes and references

1 J. Huang, B. Hu, J. Meng, T. Meng, W. Liu, Y. Guan, L. Jin and X. Zhang, *Energy Environ. Sci.*, 2024, **17**, 1007–1045.
2 H. Liu, W. Shen, H. Jin, J. Xu, P. Xi, J. Dong, Y. Zheng and S.-Z. Qiao, *Angew. Chem., Int. Ed.*, 2023, **62**, e202311674.
3 T. Jin, S. Shen, A. Xu, J. Pan, G. Zhou and W. Zhong, *Small*, 2025, **21**, 2500667.
4 Z. Yan, Z. Liu, G. Zhou, T. Jin, H. Zhang, L. Gu, T. Gao, S. Shen and W. Zhong, *Angew. Chem., Int. Ed.*, 2025, **137**, e202501964.
5 H. Du, T. Sun, M. Wang, Y. Tang, Y. Yu and J. Wang, *Chem. Commun.*, 2025, **61**, 5719–5730.
6 W. Li, H. Zhang, M. Hong, L. Zhang, X. Feng, M. Shi, W. Hu and S. Mu, *Chem. Eng. J.*, 2022, **431**, 134072.
7 S. Jia, J. Zhang, Q. Liu, C. Ma, Y. Tang and H. Sun, *J. Mater. Chem. A*, 2023, **11**, 23489–23497.
8 F. He, Y. Mao, Y. Hu, J. Wu, E. Xie, Z. Wang and Y. Li, *Chem. Commun.*, 2024, **60**, 11347–11350.
9 P. Liu, B. Chen, C. Liang, W. Yao, Y. Cui, S. Hu, P. Zou, H. Zhang, H. J. Fan and C. Yang, *Adv. Mater.*, 2021, **33**, 2007377.
10 C. Guo, Y. Zhang, M. Yin, J. Shi, W. Zhang, X. Wang, Y. Wu, J. Ma, D. Yuan and C. Jia, *J. Power Sources*, 2021, **485**, 229315.
11 J. Huang, H. Sheng, R. D. Ross, J. Han, X. Wang, B. Song and S. Jin, *Nat. Commun.*, 2021, **12**, 3036.
12 P. Ye, K. Fang, H. Wang, Y. Wang, H. Huang, C. Mo, J. Ning and Y. Hu, *Nat. Commun.*, 2024, **15**, 1–12.
13 M. Gao, J. Li, Z. Wang, Z. Yang, Y. Chen, W. Deng, W. Liang, T. Ao and W. Chen, *Sep. Purif. Technol.*, 2024, **328**, 125084.
14 R. Zhang, L. Pan, B. Guo, Z.-F. Huang, Z. Chen, L. Wang, X. Zhang, Z. Guo, W. Xu, K. P. Loh and J.-J. Zou, *J. Am. Chem. Soc.*, 2023, **145**, 2271–2281.
15 J. Wang, W. He, Y. Zong, Y. Tang, J. Wang and R. Ma, *Chem. Commun.*, 2024, **60**, 9444–9447.
16 Y. Feng, X. Wang, J. Ma, N. Wang, Q. Liu, K. Suenaga, W. Chen, J. Zhang, Y. Zhou and J. Wang, *Adv. Energy Mater.*, 2024, **14**, 2401501.
17 Y. Feng, N. Ran, X. Wang, Q. Liu, J. Wang, L. Liu, K. Suenaga, W. Zhong, R. Ma and J. Liu, *Adv. Energy Mater.*, 2023, **13**, 2302452.
18 H. Zhu, J. J. Wang, Z. Xu, Y. Tan and J. Wang, *Small*, 2024, **20**, 2404919.
19 Y. Qi, Y. Zhang, L. Yang, Y. Zhao, Y. Zhu, H. Jiang and C. Li, *Nat. Commun.*, 2022, **13**, 4602.
20 L. Li, G. Zhang, C. Zhou, F. Lv, Y. Tan, Y. Han, H. Luo, D. Wang, Y. Liu, C. Shang, L. Zeng, Q. Huang, R. Zeng, N. Ye, M. Luo and S. Guo, *Nat. Commun.*, 2024, **15**, 4974.
21 H. B. Tao, Y. Xu, X. Huang, J. Chen, L. Pei, J. Zhang, J. G. Chen and B. Liu, *Joule*, 2019, **3**, 1498–1509.
22 Y. Mei, J. Chen, Q. Wang, Y. Guo, H. Liu, W. Shi, C. Lin, Y. Yuan, Y. Wang, B. Y. Xia and Y. Yao, *Sci. Adv.*, 2024, **10**, eadq6758.